STARS

University of Central Florida
STARS

Electronic Theses and Dissertations, 2004-2019

2017

Mid-Infrared Absorption Spectrometer for Multi-Species Detection Using LEDs for Space Applications: Development and Flight Testing

Michael Villar
University of Central Florida

Part of the Aerodynamics and Fluid Mechanics Commons
Find similar works at: https://stars.library.ucf.edu/etd
University of Central Florida Libraries http://library.ucf.edu

This Masters Thesis (Open Access) is brought to you for free and open access by STARS. It has been accepted for inclusion in Electronic Theses and Dissertations, 2004-2019 by an authorized administrator of STARS. For more information, please contact STARS@ucf.edu.

STARS Citation
Villar, Michael, "Mid-Infrared Absorption Spectrometer for Multi-Species Detection Using LEDs for Space Applications: Development and Flight Testing" (2017). *Electronic Theses and Dissertations, 2004-2019*. 5497.
https://stars.library.ucf.edu/etd/5497

MID-INFRARED ABSORPTION SPECTROMETER FOR MULTI-SPECIES DETECTION USING LEDS FOR SPACE APPLICATIONS: DEVELOPMENT AND FLIGHT TESTING

by

MICHAEL S. VILLAR
B.S. University of Central Florida, 2015
B.S. University of Central Florida, 2015

A thesis submitted in partial fulfillment of the requirements
for the degree of Master of Science
in the Department of Mechanical and Aerospace Engineering
in the College of Engineering and Computer Science
at the University of Central Florida
Orlando, Florida

Spring Term
2017

Major Professor: Subith S. Vasu

© 2017 Michael S. Villar

ABSTRACT

As commercial space travel expands, the need for specialized instrumentation to ensure the safety of crew and cargo becomes increasingly necessary. Both the Federal Aviation Administration (FAA) and pioneers in the space tourism industry have expressed an interest in a robust, low cost, and low power consumption sensor to measure atmospheric composition aboard spacecraft. To achieve this goal a time-resolved NDIR absorption sensor that measures transient levels of gaseous carbon dioxide (CO_2) and carbon monoxide (CO) was developed. The developed sensor has a wide range of applications applicable to the growing needs of industry, from monitoring CO and CO_2 levels for crew cabin safety to early detection of gas leaks, fires, or other atmospheric altering events. A proof of concept, lab-bench dependent sensor has been previously developed to begin to target the needs of this industry.

This thesis discusses the expansion and evolution from this previous lab-bench dependent design into a portable, autonomous, and remote sensor that is able to withstand the harsh environmental conditions required for its intended operation in near space. The sensor incorporates compact high-efficiency LEDs that transmit in the 3-5μm wavelength range. These LEDs are further centered at 4.2μm and 4.7μm by the use of narrow band-pass filters to measure the spectral absorbance features of CO_2 and CO respectively. Active and passive thermal management of all components is achieved via thermal electric coolers (TEC) and thermal sinks to enable sensor temperature control in applicable low convection environments. To accomplish the needs for a stand-alone sensor, remote and autonomous operation is achieved via the inclusion of a real-time embedded controller with configurable FPGA/IO modules that autonomously handle thermal management, LED operation, and signal data acquisition/storage. Initial instrument validation was

completed by utilizing a thermal vacuum chamber with a testable temperature and pressure range from standard temperature and pressure (STP) down to -22°F and 8mbar. Variable measurements of $CO/CO_2/N_2$ gas mixtures were supplied via mass flow controllers to the sensor's gas cell in order to determine various key metrics of sensor operation. The culmination of the sensor's operational validation was via its flight aboard a NASA funded Louisiana State University (LSU) high-altitude balloon. This flight reached an altitude of 123,546ft with ambient temperatures and static pressures ranging from 910mbar and 53°F at ground level to .68mbar and -54°F at float altitude. A total mission time of 18h:09m:30s was reached with a total float time of 15h:08m:54s. Successful sensor operation was achieved throughout the entire mission which demonstrates the applicability, adaptability, and relevance of the technologies discussed here for space applications.

To my parents whose unwavering support and guidance throughout my life has helped make me into the man I am today.

ACKNOWLEDGMENTS

I would like to acknowledge Dr. Subith Vasu for his continual guidance and support of my work over these last two years. His knowledge and support was invaluable to me during this study. I would also like to thank my committee members, Dr. Partridge and Dr. Chow for their advisement and support during my defense.

I also need to thank those that helped work on this project with me: Justin Urso, Akshita Parupalli, Erik Ninnemann and Kyle Thurmond. All of my co-workers, whom directly or indirectly helped me over the years as well as made work a great pleasure: Zack Loparo, Joseph Lopez, Sam Barak, Leigh Nash, Owen Pryor, Sneha Neupane, Frank Barnes, and Anthony Terracciano. They were truly a great group of individuals and taught me so much during my time here at UCF.

Lastly I would like to thank the Federal Aviation Administration Center of Excellence for Commercial Space Transportation (FAA COE CST) for sponsoring this research. Nick Demidovich of the FAA COE CST has been a pleasure to partner with in this field.

TABLE OF CONTENTS

LIST OF FIGURES ix

LIST OF TABLES xi

CHAPTER 1: INTRODUCTION 1

Motivation 1

CHAPTER 2: THEORY 4

Beer-Lamberts Law 4

CHAPTER 3: SENSOR DESIGN 7

Overview of Previous Work 7

High-Altitude Balloon Flight 12

Optical Configuration 13

Data Acquisition Unit 14

Electronics Control Box Specifications 16

Temperature Control 19

Overall Sensor Power/Weight/Size 20

CHAPTER 4: VALIDATION TESTS 24

Component Validation 24

NASA CSBF Thermal-Vacuum Tests 29

High Altitude Student Payload Flight 31

CHAPTER 5: CONCLUSIONS 36

Conclusions 36

APPENDIX I: HASP FLIGHT OPERATIONS VIEW 37

HASP Flight Operations View 38

APPENDIX II: PRE AND POST FLIGHT PICTURES 39

HASP Flight Design Pre Flight [7] 40

HASP Flight Design Post Flight [7] 41

REFERENCES 42

LIST OF FIGURES

Figure 1: CO2 absorption spectrum, water absorption spectrum (x100 for visibility), and the CO2 bandpass filter. Water features negligible in this region. Features calculated at 4psia.[2] 2

Figure 2: Depiction of absorption spectroscopy in action in a target gas medium 4

Figure 3: Comparison of absorption features of CO2 at STP (left) and near space conditions (right). Absorption strength at near space may be halved or less [2]. 6

Figure 4: Spectral profile depicting LED outputs (blue lines), band-pass filters (red lines) and absorption features of CO2 and CO (at STP)[2] 8

Figure 5: Lab bench LED based absorption spectrometer previously designed by Kyle Thurmond 9

Figure 6: Alternative view of the first iteration Lab-bench sensor design[2] 10

Figure 7: Calibration curve for neat gas measurements for CO and CO_2 at STP (1atm and 24°C). 11

Figure 8: Flow chart to achieve balloon flight readiness 12

Figure 9: Schematic of sensor optical configuration [2]. 14

Figure 10: cRIO 9031 DAQ used for balloon flight. 15

Figure 11: NI cRIO Communication handling process between the sensors coding and hardware. 16

Figure 12: HASP balloon flight power schematic 17

Figure 13: Mounting location of WLD 3343 LED drivers to allow for maximum thermal dissipation. 19

Figure 14: Supplied HASP balloon flight interface plate for the LED sensor [7] 21

Figure 15: Aluminum housing box for electrical components. 22

Figure 16: Sensor optical rail mounted to side of aluminum structural casing 23

Figure 17: Modified bench top sensor placed inside the test area of a thermal vacuum chamber 24

Figure 18: Environmental chamber provided by Dr. Peale at UCF..... 25

Figure 19: LED intensities over duration of an environmental chamber test 26

Figure 20: Conversion of UCF environmental chamber testing design into HASP balloon flight design. 28

Figure 21: Finalized High Altitude Balloon Flight Design 29

Figure 22: Thermal-Vacuum testing at NASA's CSBF located at Palestine, Texas. 30

Figure 23: NASA CSBF thermal vacuum testing procedure. 30

Figure 24: HASP balloon flight path tracked over its entire mission. 31

Figure 25: High altitude balloon flight profile for sensor package. 32

Figure 26: Collected flight data of LED intensity output measured throughout the flight with ambient temperature plotted for comparison. 33

Figure 27: LED balloon flight temperature plotted against intensity with STP temperature and intensity calibration curve. 34

Figure 28: LED Calibration and post flight test configuration. 35

LIST OF TABLES

Table 1: Power consumption breakdown of HASP sensor design. 18

Table 2: HASP balloon flight constraints 21

Table 3: Ground test and flight test average power consumption 35

CHAPTER 1: INTRODUCTION

Motivation

NASA's 2015 Technology Roadmap under Technology Area 6: Human Health, Life Support, and Habitation Systems describe a few applications of a gas sensor that is low-power and lightweight enough for use in space applications. Once such application is a suitability as an atmospheric constituent sensor for portable life support systems (PLSS) that can be used in extravehicular activities (EVA's), or possibly as an early fire detection system onboard space craft or the International Space Station (ISS) [1].

NASA's Space Technology Roadmaps, Topic 6.2.2.9 covers the desire for research into the development of an in-suit atmospheric constituent sensor for PLSS. The demand would require it to be of small size and weight, have active thermal management in various environments, have a low sampling rate, maintain accuracy in a low pressure range (3 to 23psia), and maintaining immunity to humidity effects [1]. The main target gasses for this sensor design are ones related to metabolic functions, including those such as carbon dioxide (CO_2), oxygen (O_2), water vapor H_2O, and ammonia (NH_3). The developed sensor that is discussed in this paper is currently able to detect CO_2 to a 30ppm level at 1atm and can be shifted to include measurements of NH_3 and H_2O. Figure 1 below shows that CO_2 is easily detectible without interference from H_2O.

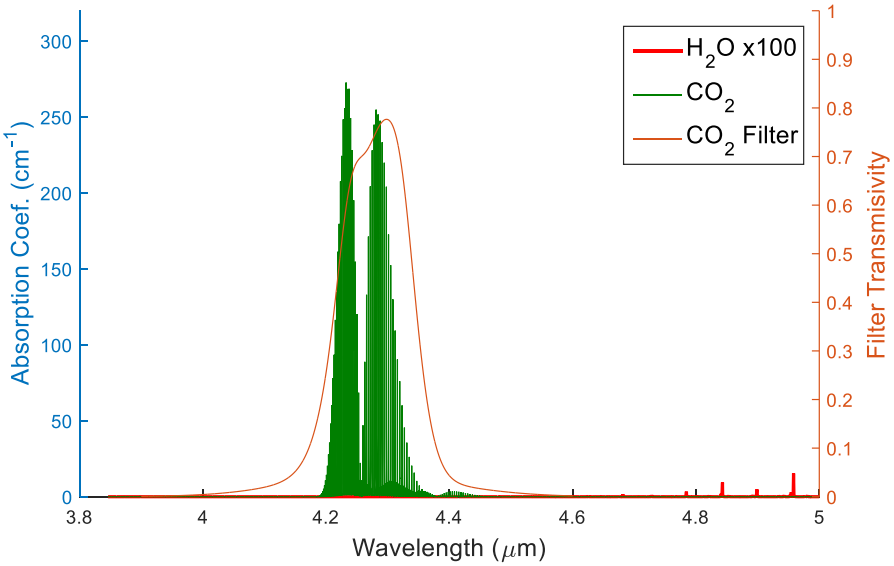

Figure 1: CO2 absorption spectrum, water absorption spectrum (x100 for visibility), and the CO2 bandpass filter. Water features negligible in this region. Features calculated at 4psia.[2]

Topic 6.4.2 on NASA's Technology Roadmap shows an important focus on fire detection and suppression [1]. The developed sensor was designed to accomplish the goal of improving the methods of detection for fire as well as an attempt to eliminate false positives. NASA's current choice for fire detection sensors is a forward scattering near-infrared laser. That sensor detects airborne particles (characteristics of smoke) to determine if an event has occurred. The drawback to their current method is that non-combustion particles can interfere with the system, creating false positives. During any long term space mission waste in the form of dust particles will accumulate in the vessel which will lead to an increasing amount of false alarms. NASA has suggested that a more robust approach would be to measure gaseous combustion byproducts (including CO2, CO, etc.) while simultaneously measuring smoke particles. Subheading 6.4.2.2 of the STR shows an interest in such a fire detection method for manned space vehicles. The technology discussed in this paper can be utilized for the development of affordable sensors that

can be distributed throughout a vessel to measure targeted combustion byproducts. The inclusion of LED's over the typical use of lasers drastically lowers the power consumption of this detection sensor while also allowing for a compact form to enable placement in targeted locations such as wire panels or near gas tanks/regulators. With low per unit costs this enables the inclusion of high redundancy in the event of component failures.

Under the directive of the FAA COE CST (Federal Aviation Administration Center of Excellence: Commercial Space Transportation), the developed fire detection sensor should extend beyond the pressurized crew cabin zones and into low pressure/temperature areas. Areas including fuel/oxidizer tank storage, cargo bays, transitional sections from partially to fully closed life support systems, etc. It is therefore desirable to have sensors that are able to operate in a wide range of environments that can be encountered in space missions. With these operational ranges in mind, sensor testing were conducted inside of environmental chambers to validate component operation. To extend this testing, a high attitude balloon flight was secured to test the designed sensor in an applicable low pressure/temperature environment.

In this work an LED-based non-dispersive infrared (NDIR) sensor was designed and adapted in preparation for a high altitude balloon flight which put the sensor technology through a trial readying it for spaceflight applications. During this process, the sensor was shown to operate in a range of environments as a demonstration of the suitability to these applications as well as to establish the base technology which may lead to a future series of sensors capable of measuring a larger range of species.

CHAPTER 2: THEORY

Beer-Lamberts Law

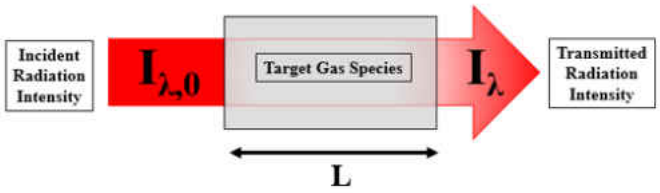

Figure 2: Depiction of absorption spectroscopy in action in a target gas medium

Absorption spectroscopy is popularly used to identify and quantify properties of a species of molecular gas by its specific absorption spectrum characteristics. Such properties include pressure, temperature and concentration. In our application we will focus on the measurement of gaseous species concentration. To achieve this a light source that emits an overlapping wavelength of the absorption spectrum of the target species is directed through it. The reduction in radiation intensity (incident radiation intensity subtracted by the transmitted radiation intensity) is measured and then correlated to the targeted gas's concentration. Monochromatic absorption spectroscopy (or the transmission of a single wavelength of radiation) follows Beer-Lamberts Law. This law shows the relation between the reduction of transmitted radiation to the specific properties of light for the absorbing species. The ratio of transmitted radiation intensity (I_0 (W cm^{-2})) to incident radiation intensity (I (W cm^{-2})) with a narrow radiation frequency ν (cm^{-1}) that is transmitted through the target species is represented by Beer's Law in a summed, spectrally integrated form:

$$\boldsymbol{T = \left(\frac{I}{I_0}\right) = \int E_\lambda F_\lambda \exp(-k_\lambda L)\, d\lambda},$$

(1)

where T (\) is the transmissivity, I (W cm^{-2}) is the transmitted radiation intensity, I_0 (W cm^{-2}) is the incident radiation intensity, E_λ (\) is the spectrally emissive profile of the LED source, F_λ (\) is the spectral transmissivity profile of the filter, k_λ (cm^{-1}) is the spectral absorption coefficient, and L (cm) the absorption path length through the gas. The spectral absorption coefficient is defined as the product $k_\lambda = S_\lambda \phi_\lambda P x_i$ where S_λ(cm^{-2} atm^{-1}) is the line strength, ϕ (cm) the line-shape function, P (atm) is the total pressure, and x_i (\) the mole fraction of the absorbing species. The line strength values for this research were determined by using the HITRAN 2012 database that yields a compiled source of spectroscopic parameters that are needed to determine and simulate the transmission of light in the species [3].

Line-strength S of a targeted absorption transition section can be denoted as a function of temperature. The expression for this function is shown below:

$$S(T) = S(T_0)\frac{Q(T_0)}{Q(T)}\left(\frac{T_0}{T}\right)\exp\left[-\frac{hcE''}{k}\left(\frac{1}{T}-\frac{1}{T_0}\right)\right]\left[1-\exp\left(\frac{-hc\nu_0}{kT}\right)\right]\left[1-\exp\left(\frac{-hc\nu_0}{kT_0}\right)\right]^{-1} \quad (2)$$

where $Q(T)$ is the partition function, E''(cm^{-1}) the lower-state energy for the transition, ν_0 (cm^{-1}) the transition's line-center frequency, T_0(K) the reference temperature corresponding to the reference line-strength, S(T_0), h is Planck's constant, c the speed of light, and k is Boltzmann's constant.

When using broadband absorption, the inclusion of multiple individual absorption transitions exist within the targeted spectral region. This can generate a mixed-regime absorbance which is beyond the linear regime as denoted by Beer's Law in Equation 1 [4]. This mixed-regime may have stronger transitions that begin to saturate at certain gaseous concentrations (in this case a mixture of CO and CO_2), while weaker transitions might remain in the linear-regime. An example

of mixed-regime absorption is shown in Figure 3 below which depicts the filtered and normalized emission of a specific LED (shown in red) and the absorbed LED emission (shown in blue). Using a path length of 7.97cm and a target species (CO_2) concentration of .2% it can be seen that a number of the stronger transitions are saturated such that the incident radiation is entirely absorbed (yielding no further contribution to sensor detectability at that wavelength). This saturation creates a non-linear response where the majority of absorption transitions move from linear to saturated as discussed by Yoo et al. [5, 6].

As can be seen in Equation 1. The strength of the absorption of the target gas is directly related to the pressure of the target species. For our applications in near space conditions (low pressure) this will reduce the signal significantly. In equation 2 it can be see that the absorption strength is also effected by the species temperature but to a much lesser extent than pressure.

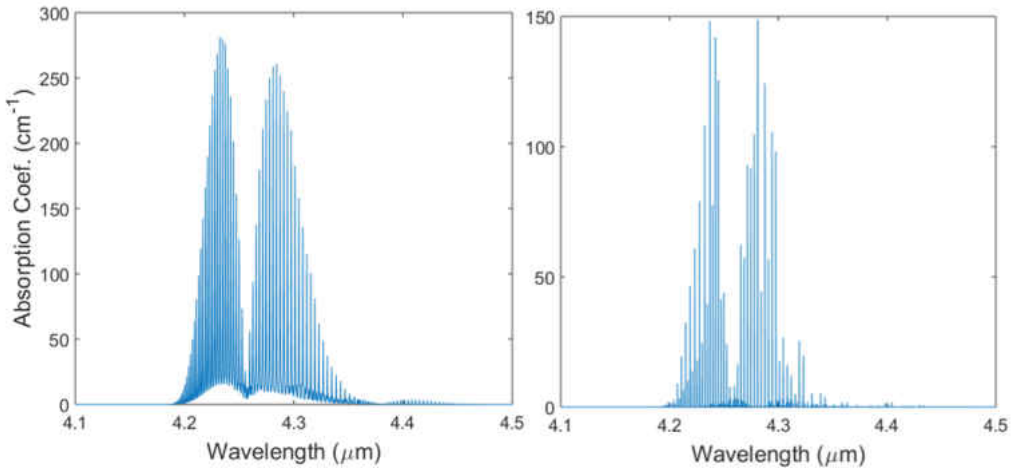

Figure 3: Comparison of absorption features of CO2 at STP (left) and near space conditions (right). Absorption strength at near space may be halved or less [2].

CHAPTER 3: SENSOR DESIGN

Overview of Previous Work

The work handed down by the previous researcher Kyle Thurmond will be outlined here. The design that was completed under his command was the fruits of a conceptual idea to create a lab-bench test version of this LED based absorption spectrometer. The sensors design has undergone extensive revision, but overall its core design has largely remained the same. Therefore this paper will repeat some necessary details then continue to discuss revisions and design changes made to ready it for a high altitude balloon flight.

NDIR sensors are attractive due to their simplicity and low-cost; they can often be built with simpler optical designs and electronics, and with much lower costs than comparable laser absorption sensors. It is common to use tungsten filament bulbs (micro-bulb) as an infrared source in NDIR sensors as they are cheap and have a relatively high output. The limitations of having significant drift, low efficiency, low modulation rates, and limited spectral range prevent their adoption for our use. The micro-bulb operates by heating a tungsten filament inside of a glass envelope to temperatures ~3000K which cause the filament to evaporate over time. This causes the output of the bulb to drift significantly which then requires regular calibration of the sensor to offset. By using LEDs in this approach, power efficient, light-weight, and stable gas sensors can be developed.

This sensor utilizes three mid-infrared LEDs to cover three different wavelength regions: a reference LED (I_0 in Beer's law) centered near 3.6μm, one near 4.2μm for detecting CO_2, and one near 4.7μm for detecting CO. Figure 4 shows the normalized spectral profiles of these LEDs

overlaid with the absorption features of CO and CO_2; it is clear from the figure below that the LEDs are spectrally broader than the individual absorption transitions, and that the associated measurements will be the integral of absorption from many individual lines in the indicated bands.

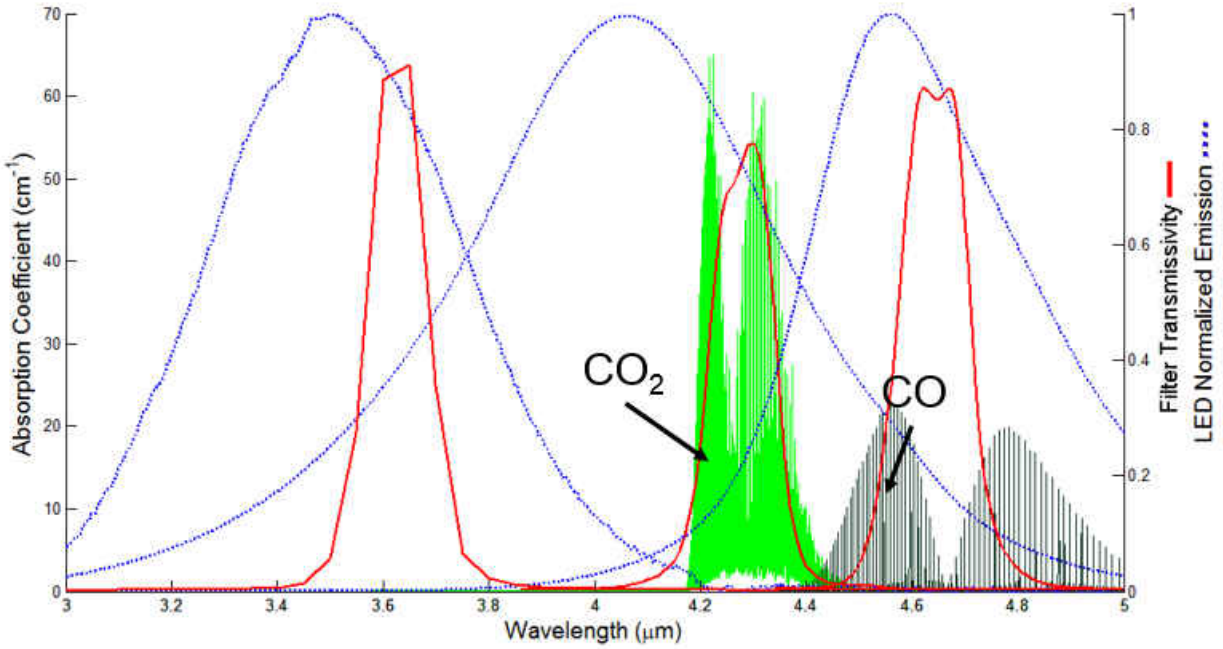

Figure 4: Spectral profile depicting LED outputs (blue lines), band-pass filters (red lines) and absorption features of CO2 and CO (at STP)[2]

The overall system was broken into three major subsystems; the source, probe and collector. Figure 5 shown below depicts these bench top subsystems. The source houses the three LED's centered at their three unique spectral emissions which are then collimated, filtered, combined and focused onto the optical path. That light is then guided along the optical path and through the probe where gaseous species in the absorption cell are sampled. The transmitted light then continues to the collector. The collector contains the photovoltaic detector to measure the transmitted light that exits the probe.

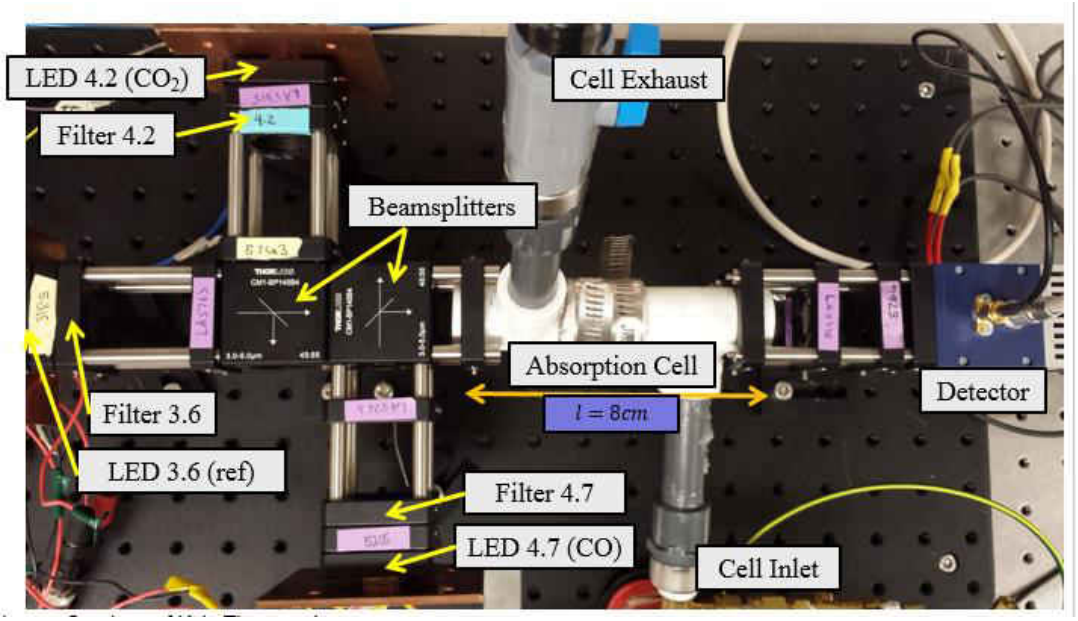

Figure 5: Lab bench LED based absorption spectrometer previously designed by Kyle Thurmond

An alternate view of the previous sensor design is shown below in Figure 6. As you can see it is bound to an optical table and requires multiple power supplies to source the electrical components as well as mass flow controllers and function generators to modulate the LED's. The limitations of this design made it ill-suited for use in its intended space applications. This paper covers how this initial prototype was environmentally hardened and converted into a portable and autonomous sensor.

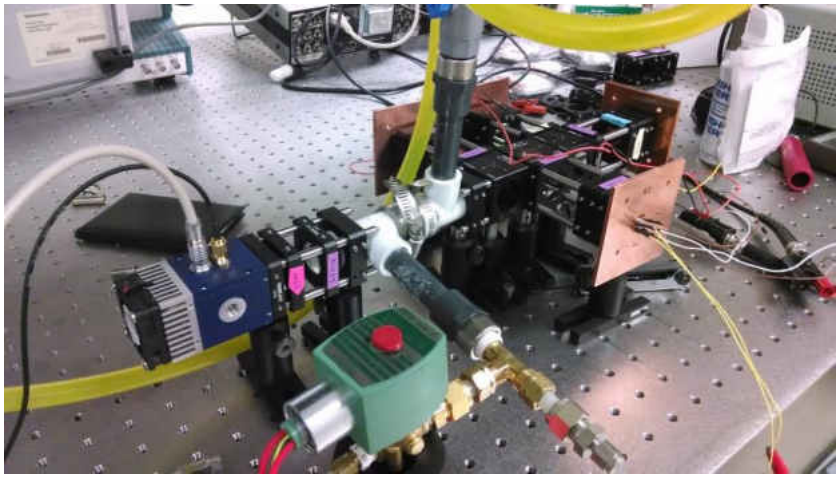

Figure 6: Alternative view of the first iteration Lab-bench sensor design[2]

Sensor performance was evaluated at standard temperature and pressure (STP). In this paper, STP is considered 1 atm and 24°C. STP measurements have previously been assessed however some optimizations to the electronics have increased the performance, so reevaluation is discussed here. Since these modifications do not impact cross-species interference or bandwidth, these tests were not repeated. All concentrations measurements were made using a simple flow cell which was constructed of PVC pipe and sapphire windows. Neat bottled gas standards and Alicat Scientific mass flow controllers were used to control the measurement gas composition (standards included 10% CO_2 and 10% CO, all in N_2 balance). Single-gas calibration curves were measured by diluting the standards with ultra-high purity nitrogen; each gas was stepped from 0% to 1% in 0.1% intervals, and from 0% to 10% in 1% intervals. Two measurements were taken at each gas composition setting: one while stepping up the concentration of the standard and one while stepping down; lack of hysteresis between the two data sets confirmed that the cell reaches steady state at each composition element of the calibration scan.

Neat gas measurements at STP are shown below in Figure 7. This response deviates from the linear output predicted by Beer's law (under the assumption of spectral narrowness) and typical narrow-band (e.g. laser-based) absorption however it is typical of broad spectrum multi-feature absorption. [5, 7]. The detection of each gas, defined as the concentration where the signal-to-noise ratio (SNR) is unity (signal = 2-σ), was previously determined to be 30ppm for CO_2 and 400ppm for CO with an 8 cm path length.[2] From that experiment set, the electronics had been updated to provide more current to the LEDs and the gas mass flow control methods have changed. The updated electronics resulted in an improved detectivity limit for each gas of 8ppm for CO_2 and 300ppm for CO.

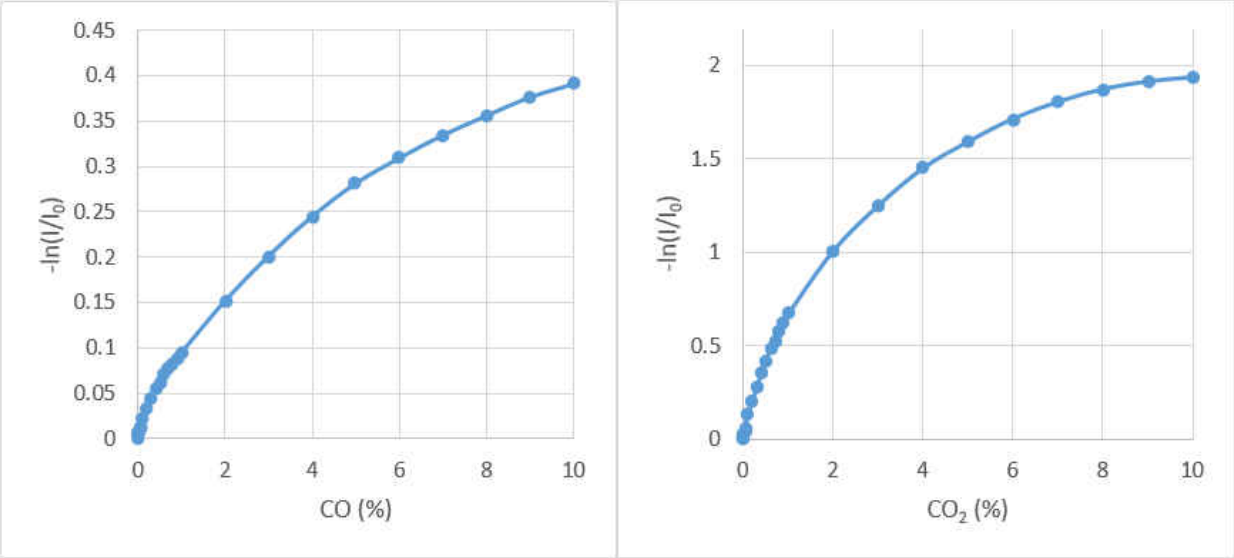

Figure 7: Calibration curve for neat gas measurements for CO and CO_2 at STP (1atm and 24°C).

High-Altitude Balloon Flight

To further verify the systems capabilities, a high-altitude balloon flight was secured to allow for validation of the sensors function in a non-simulated environment. The balloon flight secured was the High Altitude Student Platform (this point on will be referred to as HASP) out of LSU. The HASP program was initially created to provide flight opportunities for experiments that fall in-between short range sounding balloons and long range orbital satellites. The HASP platform itself is a support structure for 12 experimental payloads. These 12 payloads are broken up into 4 "large" payloads with maximum weight of 20kg and 8 "small" payloads with a maximum of 3kg. The NDIR sensor in this paper was chosen for one of the large payload spots. The HASP support platform supplies standard interfacing for power, telemetry and discrete commands for all 12 payload seats. The polyethylene helium filled balloon reaches a peak altitude averaging around 120,000ft and has a total mission time ranging from 12 to 26 hours.

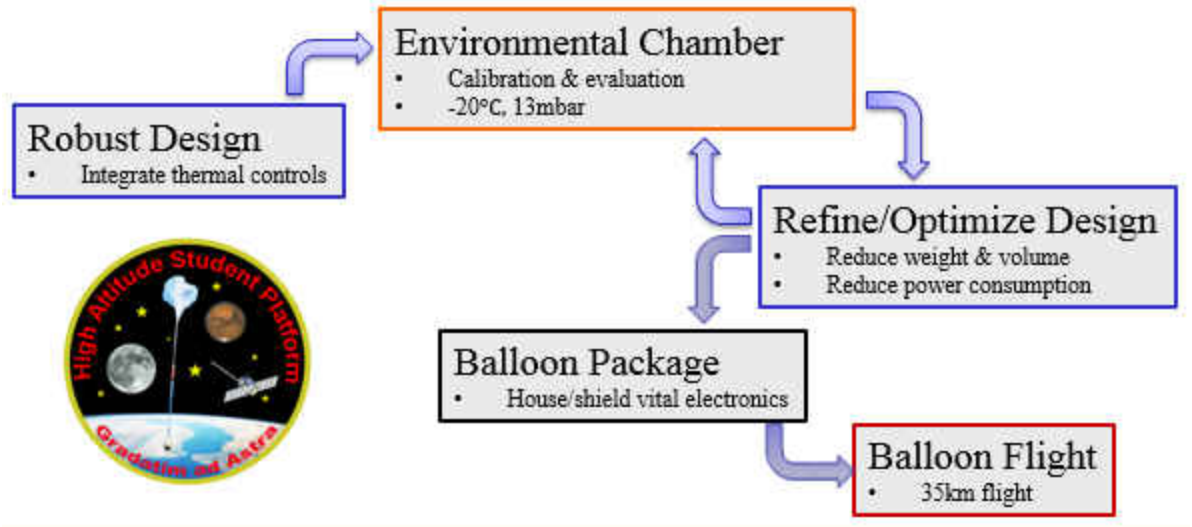

Figure 8: Flow chart to achieve balloon flight readiness

Figure 8 above depicts a flow chart on how the sensor evolved from its initial bench top design to a robust and autonomous package. An initial robust design was put forth that was then vetted and evaluated in an environmental chamber. Over consecutive tests in this chamber revisions were completed to reduce overall weight, volume and power consumption. At the end of this revisional process a flight worthy design was achieved and was integrated into the balloon flight chassis to fly on the HASP flight.

Optical Configuration

The three LEDs used are multiplexed into a single signal path so that only one detector is necessary to reduce cost and complexity associated with multiple detectors. Multiple detector require accounting for the detector-specific response, dark current, noise and other characteristics. Each LED is individually collimated, filtered with the appropriate band-pass filters, and combined using two Pellicle beamsplitters as shown in Figure 9. The output of each LED was modulated at a unique frequency by the dedicated data acquisition unit (DAQ), using a square-wave unity-duty-cycle function. The specific frequencies were 5, 7 and 11 kHz for the 3.6µm, 4.2µm and, 4.7µm LEDs respectively.

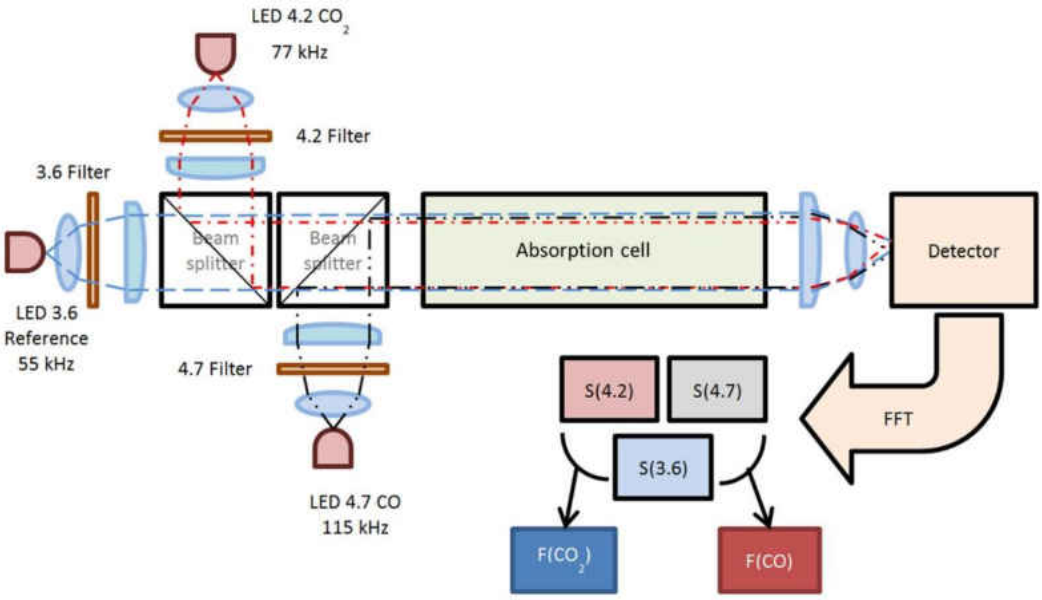

Figure 9: Schematic of sensor optical configuration [2].

In the previous design, the LEDs were driven using function generators (each were driven by an individual unit) however these did not meet the power requirements of the LEDs (~0.5V, 1A pulsed). In this design, both the LEDs and TECs were driven using Wavelength Electronics WLD3343 general purpose driver which increased the output of the LEDs.

Data Acquisition Unit

The data acquisition system that was flown on the balloon flight was the National Instruments cRIO-9031 DAQ. The cRIO-9031 is a rugged high performance controller that was chosen as it is designed to operate in harsh conditions like those that will be introduced during flight operation. It is able to withstand a max shock of 50g and operate at temperatures ranging from -40 to 70°C.

Figure 10: cRIO 9031 DAQ used for balloon flight.

The cRIO was selected to allow for multiple sensor inputs (photodetector, thermocouples, barometer, etc.), analog outputs for controlling LED function while also utilizing digital outputs for TEC control. The cRIO DAQ was programed such that when powered on will start up the written FPGA system control VI (Overview architecture of current lab run VI shown in Figure 11). This controls the LED function outputs, collects and stores data, and monitors and controls LED temperatures via thermocouples/TECs.

At the start of HASP launch, a single power up command will be sufficient for the entire payload flight operation. On power up, the National Instruments cRIO Data Acquisition System (DAQ) will boot and automatically begin data collection/storage and will remain powered for the entire operation. Data will be collected at a constant timed interval and will be stored in onboard memory for post processing after landing.

An example of system operation is shown below in an architecture overview. The Real Time VI runs the programing loops that send commands to and from the FPGA VI. The RT VI handles LED temperature control, data streaming/logging and is interfaced with the HASP mainframe via a RS-232 data cable to collect and record GPS and time data. The FPGA handles communication to the hardware I/O's. A client VI is currently in use (not shown) for system monitoring while it is in use in a laboratory setting. For flight operations the Client VI is removed data is directly stored in onboard memory for post processing after flight operation. The cRIO DAQ was used to make the system fully autonomous which included signal generation, temperature control, and periodic sampling.

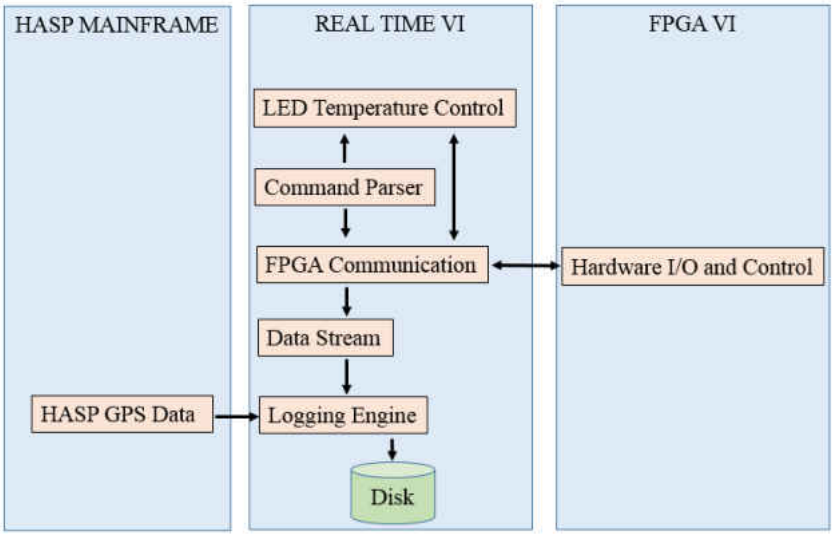

Figure 11: NI cRIO Communication handling process between the sensors coding and hardware.

Electronics Control Box Specifications

The HASP support frame provides power that is supplied over a range of 29-32 volts (averaging at 30V output) for roughly 270 amp hours (power specifications tested at 20C). This power is generated from an 11 cell lithium battery pack. This power system was designed by following the

ATIC (Advanced thin ionization calorimeter) experimental design which allows for hot swapping components as necessary. The ATIC concept runs a 30V bus to each section and local voltage conversions are done to desired power. Each of the 12 payload seat interfaces includes imbedded relays to enable flow control of power (realized in the form of discrete on/off signal commands).

Shown below in Figure 12 is the general interface between the HASP provided power source and the sensor payload HASP provides ~ +30 VDC that will be down regulated to +24 VDC to power NI-cRIO DAQ, this is then further down regulated to + 6VDC to power the LED/TEC Electronics Board and the Detector Board. Figure 12 shows the overall circuit schematic for LED/TEC control. The +6 VDC powers the LEDs and TECs directly. LED/TEC Signal control is powered and modulated by a regulated +5 VDC line from the NI-cRIO DAQ.

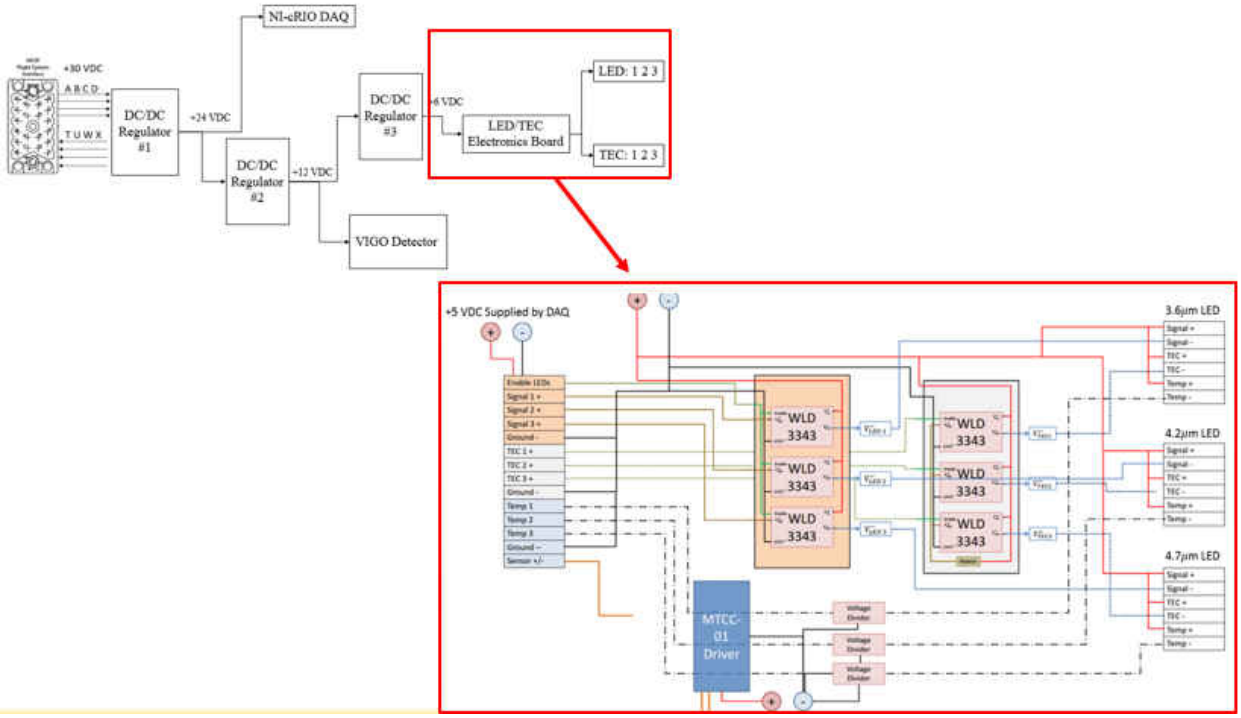

Figure 12: HASP balloon flight power schematic

Table 1 shows the power draw breakdown (in watts as well as volts and current) per component as well as the total maximum power consumption of the payload. Total nominal power draw is just over 34W of power. The detector has a total power consumption of 5.5W the LEDs (of which there are 3) uses a total power of 1.215W. The TECs that control the LEDs temperatures (they are integrated inside of the LED casing) consumes 5.34W of power. The driving electronics uses a total of 3.03W and lastly the controlling cRIO-9031 DAQ uses 19W. The largest power draw, as can be seen, is the cRIO DAQ pulling over two thirds of the power.

Table 1: Power consumption breakdown of HASP sensor design.

Component	Quantity	Unit Power, W	Total Comp Power, W
Detector	1	5.5	5.5W
LED	3	.405	1.215W
TEC for LED	3	1.78	5.34W
Driving Elec.	1	3.03	3.03W
cRIO-9031	1	19	19W
		Total:	34.086W

The LED/TEC electronics board is comprised of the WLD 3343 laser diode drivers and the interfaces from the DC/DC regulators to the LED's themselves. These WLD drivers were selected because they allow for a high switching frequency of the LEDs to enable signal multiplexing. A second set of WLD 3343 drivers were chosen specifically to act at solid state relays for the activation and deactivation of the thermal electric coolers (TEC's) imbedded on the LED's themselves. These drivers are bolted to the side place of the electronics case to maximize the volume of the thermal sink to help in heat dissipation. The attachment of these drivers is depicted in **Error! Reference source not found.** below.

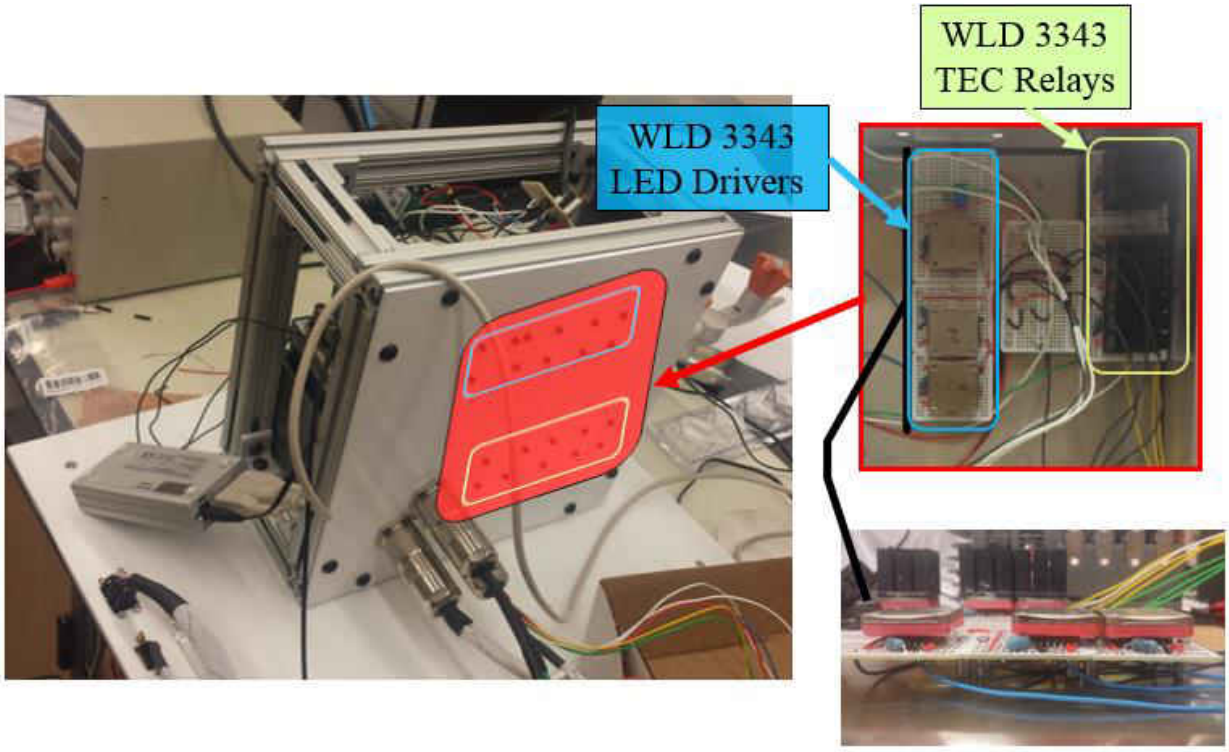

Figure 13: Mounting location of WLD 3343 LED drivers to allow for maximum thermal dissipation.

Temperature Control

While this sensor is designed to operate in multiple environments, the greatest challenges in thermal management is operation in low pressures as heat rejections is greatly reduced due to low heat convection. All critical components (each individual LED and the photodetector) have their own individual optimal operating temperatures and as such are each individually equipped with thermal electric coolers (TECs). These imbedded TECs are used to regulate the temperature of each component. Encountered temperatures at flight altitude may be lower than the optimal temperatures for each component and as such the equipped TECs may be operated in reverse. This will heat each component to optimal operating temperatures. For the detector, only cooling is active since its operating temperature is below all environmental temperatures being considered

(detector operating temperature is -60°C). The LEDs and detector are tiny masses and require very little to maintain their temperature.

The TECs will draw/disperse heat to/from the larger thermal mass of the systems body to operate (adequate contact surface has been designed to allow for sufficient conduction to and from the TECs at each location). Non-critical components have been selected such that they will perform all necessary functions without any active thermal protection. Simulations were conducted and allowances for special considerations were done to maintain optimal performance throughout operation. While the sensor and accompanying balloon package was being developed extensive testing was done inside of an environmental chamber to reduce any component failure during the balloon flight. The environmental chamber used to test the system can produce sustained conditions near what is encountered at 36km (-20°C and 13mbar).

Overall Sensor Power/Weight/Size

The HASP balloon flight provides an interfacing plate to affix the sensor to the larger balloon package. The plate supplied is shown below in Figure 14. The plate is manufactured from .25in thick PVC and includes a data connection and wiring for electrical interfacing.

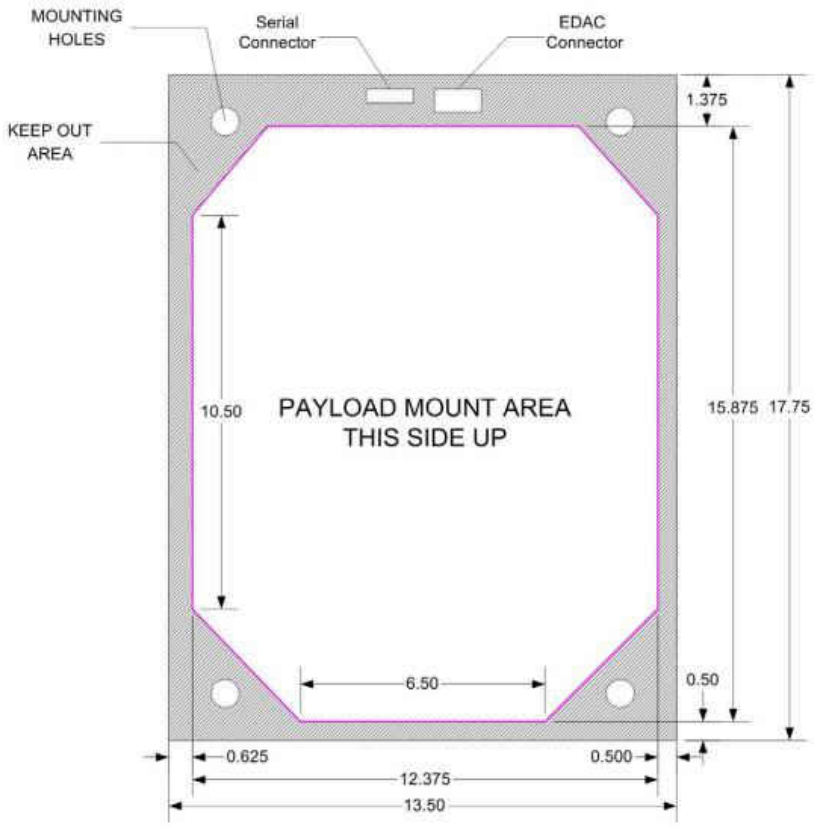

Figure 14: Supplied HASP balloon flight interface plate for the LED sensor [7]

All components attached to the mounting plate including the sensor, supporting components, nuts/bolts, etc. needed to be included in the total weight budget. The size of the allowable length/width/height is given in Table 2.

Table 2: HASP balloon flight constraints

HASP Design Constraints	
Maximum Weight	44lb
Maximum Footprint	~15in x 12in
Maximum Height	~12in
Supplied DC Voltage	29-33 VDC
Available Max Current	2.5 Amps @ 30 VDC
Discrete Commands	Power On, Power Off
Temperature Range	-60°C to 50°C
Pressure Range	6mbar to 1bar

An aluminum package was constructed shown in Figure 15Figure 15: Aluminum housing box for electrical components. to house its critical electronics (DAQ, driving electronics, batteries) which protects it from the environment and electromagnet interference (EMI) from the balloons telemetry systems, and also provides structural support upon landing.

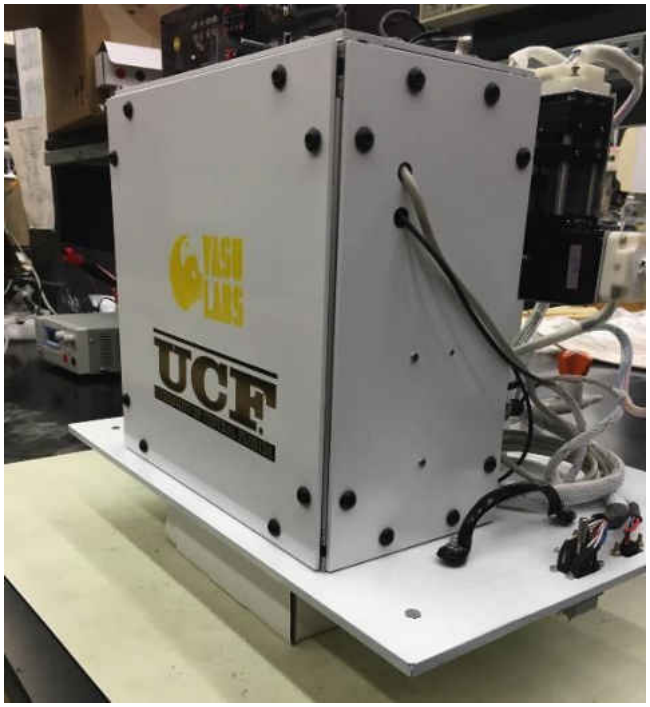

Figure 15: Aluminum housing box for electrical components.

The lens train was constructed using common lens rail systems which was further reinforced with aluminum sheet metal to mitigate misalignment. This lens train was then affixed to the side of the aluminum package as shown below in Figure 16. The wiring to each of the LED's can been seen, each bundle is 6 core strand that includes lines for the LED enable/disable, TEC operation, and built in thermistor reading for real time temperature measurements of each individual LED.

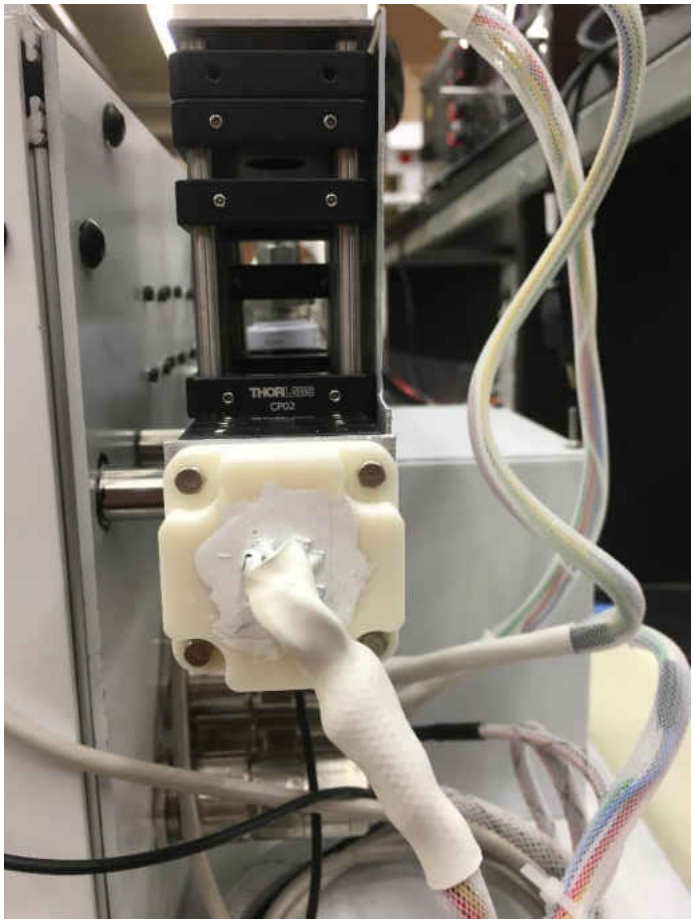

Figure 16: Sensor optical rail mounted to side of aluminum structural casing

CHAPTER 4: VALIDATION TESTS

Component Validation

Modifications of the bench top sensor design was done to allow it to be placed inside a thermal vacuum chamber to validate component operation in simulated near space conditions. The two major focuses in these tests were to monitor component temperatures over long durations and to see LED performances under vacuum. The goal was to be able to successfully state that each component integrated into the flight design was proven to operate under simulated conditions that would be experienced during the balloon flight. Thermal runaway was a major concern for some components, as heat is generated on electrical subsystems. Without the aid of convection, thermal buildup can occur. Over long periods of time this can lead to components exceeding maximum operating temperatures and would eventually result in a system failure. By validating each component over long duration tests to monitor thermal properties this failure can be avoided.

Figure 17: Modified bench top sensor placed inside the test area of a thermal vacuum chamber

An environmental chamber was used in evaluating the sensor's performance at simulated near space conditions. The chamber consists of a large steel bell jar that is 0.5m in diameter and 0.8m in height. Inside the bell jar is a copper shroud wrapped in copper tubing which allows the flow of liquid nitrogen (LN_2) which cools the interior vacuum chamber to approximately -20°C. A high volume roughing pump is used to pump the chamber down to approximately 2Torr. Further details of its construction may be found in the paper by Peale et al. [8].

Figure 18: Environmental chamber provided by Dr. Peale at UCF

The intent of this experiment is to prepare the sensor for the high altitude balloon flight in September where it will reach an altitude of up to 35km where it can see conditions of -40°C and 1/100atm (7.6Torr). The primary concern is proper thermal control of critical components at low pressure which the chamber was successfully able to replicate.

The first round of testing in the chamber was solely with the sensor to confirm everything operated as expected. This was also the first time the TECs were to be operated in reverse. The test ran for an hour with successful steady LED magnitudes as depicted in Figure 19 below. The LEDs and detector thermal management plan was very successful. However, another test was run without cooling the chamber (ambient temperature, low pressure), and it was discovered that the driver modules had trouble maintaining their temperature. This problem was solved by affixing the driver modules to a larger thermal mass as shown in the electronics control box specifications section in Chapter 3.

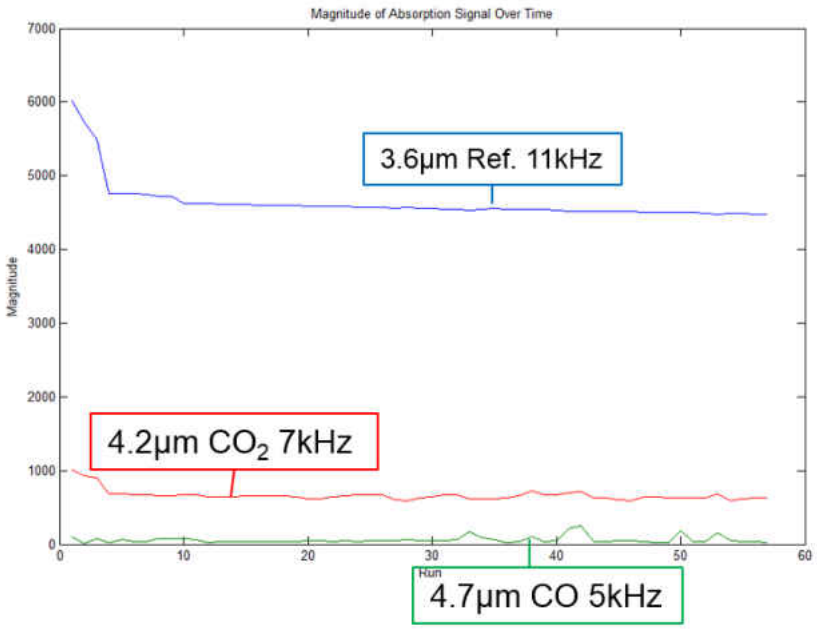

Figure 19: LED intensities over duration of an environmental chamber test

Further environmental chamber evaluations were conducted to harden the sensor design and establish calibration curves for relevant conditions. The system must maintain the LEDs and detector at a stable temperature (±0.2°C) so consistent performance is delivered and the remaining electronics (DAQ, driving modules, etc.) remain in safe operating temperature range. Each of these

critical components were therefore equipped with a temperature sensor for monitoring. During low-pressure, low-temperature operation the sensor system was able to operate as designed. Each LED maintained its temperature at -10°C within tolerance; the detector functioned optimally, and all electronics remain within safe temperature limits. The system was given an hour to reach steady state and continued to hold this standard. The mass of the LED itself is very small (~0.4), minimal energy is put through the LED (~0.5W), and with its high efficiency made temperature control requirements fairly minimal and thus one of the significant appeal of LEDs. The analysis for the detectors is similar as the LEDs do not produce a great enough energy to heat the detector. A similar evaluation was undergone under low-pressure only, without cooling. Temperature control of the LEDs and detector appeared to be unaffected however regulation of the driving modules temperature became difficult as its temperature slowly exceeded safe limits. In general, while the modules meet the design requirements of the current flight, further iteration may be required as they have substantial power requirements and generate a considerable amount of heat, adding an additional temperature monitor.

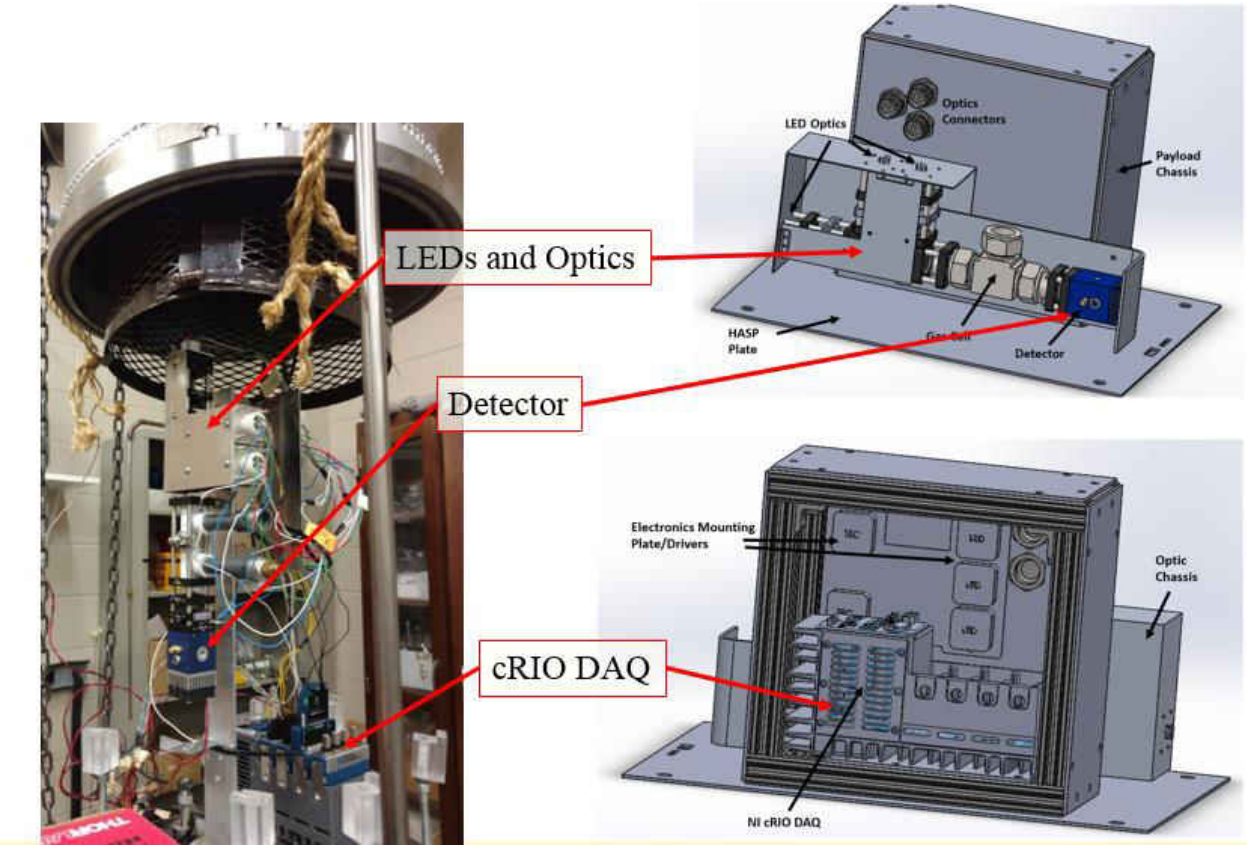

Figure 20: Conversion of UCF environmental chamber testing design into HASP balloon flight design.

After the completion of the environmental chamber study at UCF the validated components needed to be integrated into the HASP balloon flight design. Shown above depicts how each subsystem was integrated onto the HASP package. The cRIO DAQ along with the other components are enclosed inside the aluminum electronics box to shield it from the harsh environment. The LED and optical arrangement was placed on the back side of the electronics box. The finalized version of this HASP design with the completed balloon flight sensor design is shown below.

Figure 21: Finalized High Altitude Balloon Flight Design

NASA CSBF Thermal-Vacuum Tests

The second iteration of environmental chamber testing was completed at NASA's Columbia Scientific Balloon Facility's Thermal Vacuum Chamber located in Palestine Texas, as is shown in Figure 22 below. The test duration was 8 hours and 30 minutes. The temperature range was -60°C to 50°C and the pressure range was 8mbar to 1bar. Throughout the test, the system performed as expected except for a small issue involving downlinking random noise. It was discovered that this was due to the fact that one regulator was non-isolated; replacing it with an isolated regulator resolved this problem.

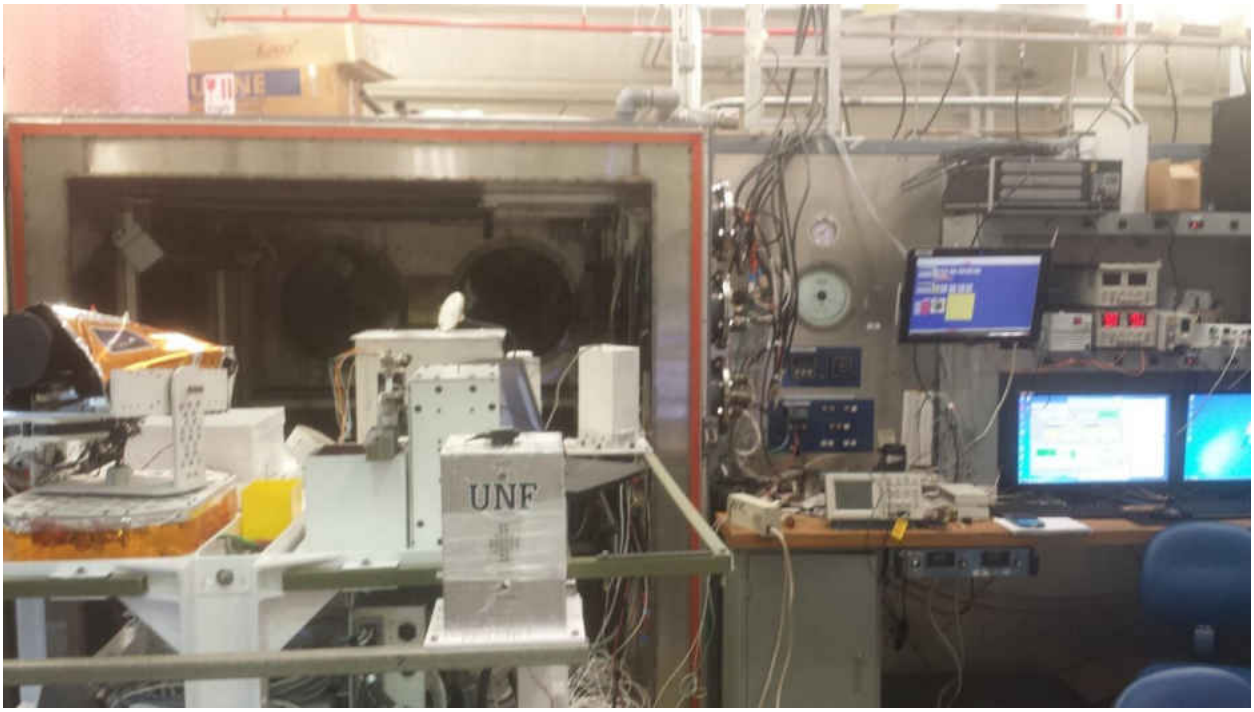

Figure 22: Thermal-Vacuum testing at NASA's CSBF located at Palestine, Texas.

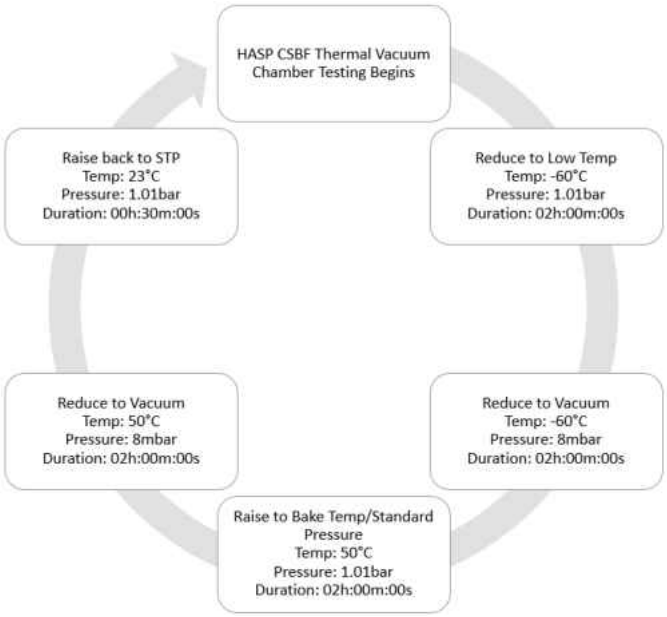

Figure 23: NASA CSBF thermal vacuum testing procedure.

High Altitude Student Payload Flight

For the balloon flight the test cell was filled to 1atm with a gas mixture of 89.51% N_2, 4.97% CO, and 5.52% CO_2 with a total cell volume of 1.7948 in^3. The cell contains a built-in diaphragm that keeps internal cell pressure equal to ambient pressure. This allowed for varying pressure measurements throughout the duration of the flight while removing the issue of having a pressurized cell at the flight altitudes. The sensor was launched on September 1st and reached a max altitude of 123,546ft over an 18 hour flight. The flight conditions are recorded below in Figure 24. The total flight duration could have been extended well into the 20+ hour range but due to wind speeds there was concern that the payload would drift too close to California and ultimately the Pacific Ocean, so an executive call was made to end the flight at the 17 hour mark to allow for proper time for descent.

Figure 24: HASP balloon flight path tracked over its entire mission.

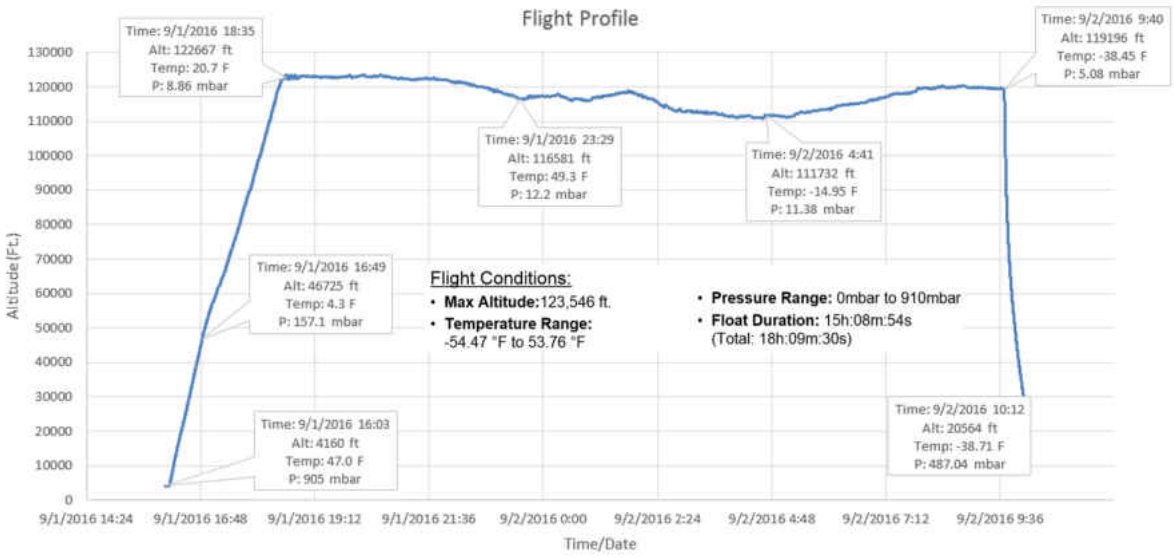

Figure 25: High altitude balloon flight profile for sensor package.

The HASP balloon flights initial attempt at launch was on August 30th. Flight ready checks began at 6am. After four hours of checks the launch was scrubbed due to poor weather conditions. A second attempt at launch was made on August 31st but was also scrubbed. Finally on September 1st with flight checks beginning at 3am the HASP package was rolled out onto the launch pad post flight check at 8am where the balloon was filled and cleared for launch. Official launch time was at 10:08am MDT on September 1st. UCF's payload was successfully returned post flight on Sept. 14th. A breakdown of the system was completed to access the onboard flight data. This included writing a Matlab script to parse all of the 697 collected measurements (1 measurement every 2 minutes over 23 hours) and correlate the peak intensities of the captured LED signals with the environmental data (Pressure/Temp) throughout the entire flight. The sensor modulated its three LEDs at different wavelengths so that a FFT could be done to the stored signal to determine the peak intensity of each LED. The peak intensities of each LED cross referenced with ambient temperature is shown below in Figure 26 and Figure 27.

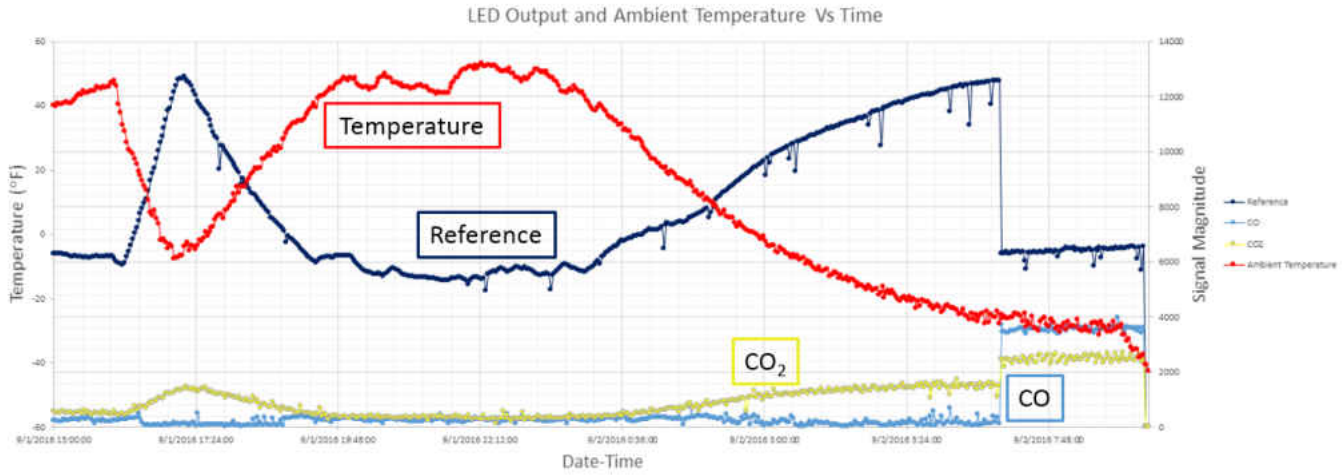

Figure 26: Collected flight data of LED intensity output measured throughout the flight with ambient temperature plotted for comparison.

The TECs under standard operation should keep the LEDs at a constant set temperature of 0°C. The actual temperature profile is shown below. A clear direct correlation of LED intensity and ambient temperature can be seen. Due to the fact that each LED's output varies with temperature a calibration equation has been established to eliminate the temperature variance in the measurements. This calibration line is shown in Figure 27 below and indicates that although the LED's were not held at constant temperature during flight, they still followed the expected temperature-intensity curve.

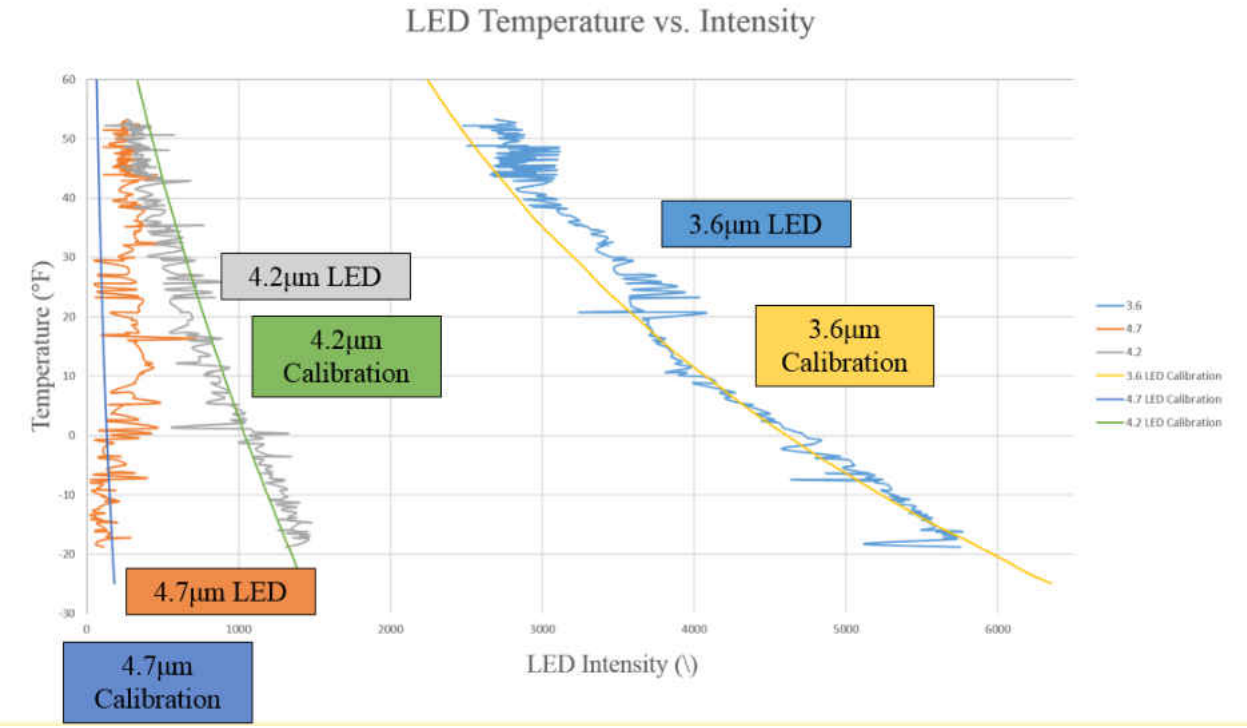

Figure 27: LED balloon flight temperature plotted against intensity with STP temperature and intensity calibration curve.

The system was placed back into the environmental chamber to test to make sure that the systems LED's post flight measurements were consistent with pre-flight measurements (LED outputs pre-flight and post-flight were found to be equal). This was established to provide confident that the tests for the temperature variance calibration equation would be applicable to the flight data. Equal pre- and post- flight LED output measurements proved that the system did not alter during flight.

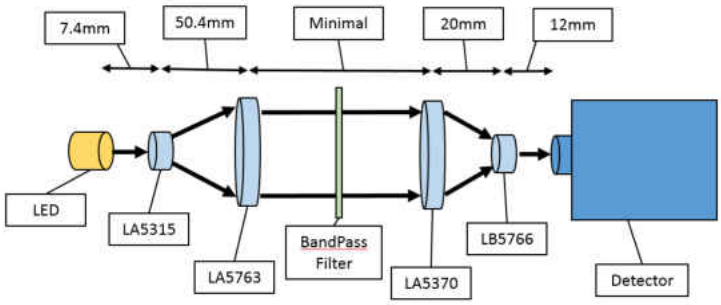

Figure 28: LED Calibration and post flight test configuration.

Analysis of the calibration curves for the LEDs shows that the 3.6 and the 4.2 roughly follows the data collected from the flight. But when looking at the 4.7 LED the intensities hardly follows the calibration. After post flight analysis of the payload, it is assumed to source from the 6VDC line from the DC/DC regulator. Shown below is a chart of the ground test power average and the flight test power average. There is a 5.1W drop in power consumption between the two scenarios, even though the payload was in the exact environmental conditions. The drop in power consumption is assumed to stem from a poor solder connection on the 6VDC converter. With the 4.7 LED already having a low starting signal to noise ratio. Further compounded with a reduced power supply made it highly susceptible to sensor noise and thus the deviation from the calibration curve. This follows as the 3.6 is the strongest LED (magnitude outputs of a minimum of 10x that of the 4.7) it is less susceptible to noise.

Table 3: Ground test and flight test average power consumption

Ground Test Average		Flight Test Average	
Voltage (V)	29.9	Voltage (V)	29.688
Current (I)	1.14	Current (I)	.976
Power (W)	34.086	Power (W)	28.986
Total Power Lost (W)		5.10	

CHAPTER 5: CONCLUSIONS

Conclusions

Current development of the sensor is undergoing an adaptation for space vehicles and any environments that may be encountered during space flight. A high altitude balloon flight has been secured which will allow evaluation of the sensor at altitudes of 35km (-40°C, 1/100atm). Additional flights are planned to follow and may also include parabolic flights or missions to the International Space Station (ISS). The goal is to develop the hardware so that it is rugged and a viable technology for a variety of sensor applications in a variety of environments. It is, therefore, crucial that the hardware can reject heat at low pressures, survive the low-temperature operation, have low drift (stable output), remain low power, and be insensitive to humidity.

Our results under simulated environmental conditions have shown that LEDs are remarkably easy to operate and maintaine at optimal temperatures during service. The bulk of diffulty encountered in both temperature and power management came from the modules used to drive the LEDs which were selected for rapid development and simplicity. Coupling this with low-power overhead and long-life (high stability) make this technology of great appeal to aerospace applications. As the hardware is further refined, it should become more compact with more efficient multiplexing approaches. This may take the form of tightly spaced arrays of LEDs which use custom integrated lenses. The driving electronics will also need to be refined to a more efficient design as the current system produce excessive waste heat.

APPENDIX I: HASP FLIGHT OPERATIONS VIEW

HASP Flight Operations View

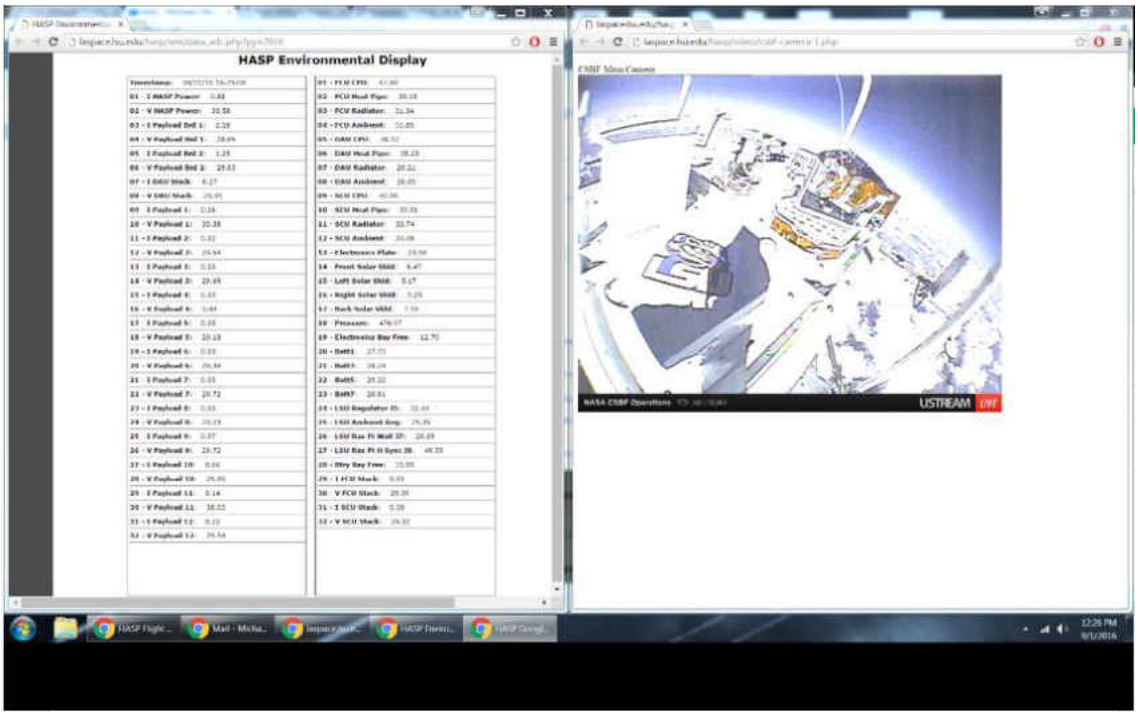

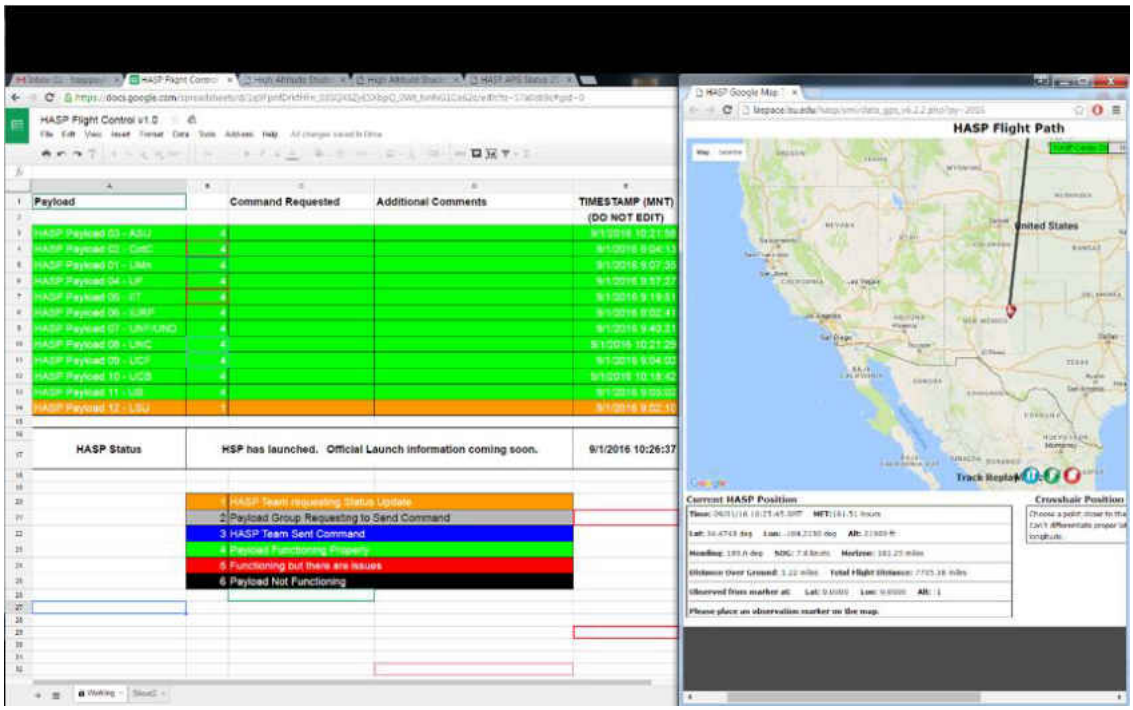

APPENDIX II: PRE AND POST FLIGHT PICTURES

HASP Flight Design Pre Flight [7]

HASP Flight Design Post Flight [7]

REFERENCES

1. Chandler, F., Ambrose, R., Biegel, B., Brown, T., Carter, J., Culbert, C., Edwards, C., Fox, J., Glaessgen, E., Hurlbert, K., Israel, D., Johnson, L., Kliss, M., Linne, D., Meador, M., Mercer, C., Meyer, M., Motil, B., Munk, M., Nesnas, I., Prince, J., Ryan, R., Scott, J., and Siochi, E. *2015 NASA Technology Roadmaps*. 2015; Available from: http://www.nasa.gov/offices/oct/home/roadmaps/index.html.

2. K. Thurmond, Z.L., W.P. Partridge Jr., S. S. Vasu, *A Light-Emitting-Diode (LED) Based Absorption Sensor for Simultaneous Detection of Carbon Monoxide and Carbon Dioxide.* Applied Spectroscopy, 2016. **70**(6): p. 962-971.

3. Rothman, L.S., Gordon, I. E., Babikov, Y., Barbe, A., Benner, D. C., Bernath, P. F., Birk, M., Bizzocchi, L., Boudon, V., Brown, L. R., Campargue, A., Chance, K., Cohen, E. A., Coudert, L. H., Devi, V. M., Drouin, B. J., Fayt, A., Flaud, J. M., Gamache, R. R., Harrison, J. J., Hartmann, J. M., Hill, C., Hodges, J. T., Jacquemart, D., Jolly, A., Lamouroux, J., Roy, R. J. L., Li, G., Long, D. A., Lyulin, O. M., Mackie, C. J., Massie, S. T., Mikhailenko, S., Müller, H. S. P., Naumenko, O. V., Nikitin, A. V., Orphal, J., Perevalov, V., Perrin, A., Polovtseva, E. R., Richard, C., Smith, M. A. H., Starikova, E., Sung, K., Tashkun, S., Tennyson, J., Toon, G. C., Tyuterev, V. G., Wagner, G., Müller, H., and Smith, M., *The HITRAN2012 molecular spectroscopic database.* Journal of Quantitative Spectroscopy and Radiative Transfer, 2013.

4. Matveev, B.A., et al., *Mid-infrared (3-5 μm) LEDs as sources for gas and liquid sensors.* Sensors and Actuators B: Chemical, 1997. **39**(1–3): p. 339-343.

5. J. Yoo, V.P., J. E. Parks, A. Perfetto, S. Geckler, W. P. Partridge, *Fast Spatially-Resolved EGR Distrubution Measurements in an Internal Combustion Engine using Absorption Spectroscopy.* Applied Spectroscopy, 2015. **69**(9): p. 1050-1061.

6. Ioffe, I. *LEDs for the mid-infrared region of the spectrum (2-6 micrometers)*. 2013; Available from:

http://www.ioffeled.com/index.php?option=com_content&view=article&id=52&Itemid=103.

7. T. Guzik, D.G., M. Stewart *2016 LSU High Altitude Student Platform* 2016; Available from: http://laspace.lsu.edu/hasp/.

8. Maukonen, D., et al. *Planetary Atmospheres Minor Species Sensor (PAMSS)*. in *SPIE Sensing Technology+ Applications*. 2014. International Society for Optics and Photonics.